Radar Backscatter from Mars: Properties of Rock-Strewn Surfaces

Bruce A. Campbell

Center for Earth and Planetary Studies, Smithsonian Institution, Washington, DC
E-mail: Bruce.Campbell@nasm.si.edu

Rock-strewn surfaces are apparently common on Mars, and radar backscatter data offer the most direct means for remotely estimating their statistical properties. This paper examines the height statistics of power-law and exponential rock size-frequency distributions, and demonstrates the dependence of root-mean-square (rms) height on horizontal scale as a function of the distribution parameters. In general, strewn surfaces have an inherent variation in roughness for horizontal length scales below the maximum rock diameter. This leads to variations in radar echo power with wavelength, even when the differential diameter function has an inverse-cubed power-law form. Size-frequency data for a rock-strewn test site in Hawaii are consistent, over a specific range of horizontal scales, with a power-law distribution. An exponential form, while better describing the rapid decline in rock abundance above a certain size threshold, underestimates the population at the smaller scales most relevant to radar scattering. Rock sphericity statistics, often cited in descriptions of rocky areas, appear to be consistent with a Rayleigh distribution of major and minor axis diameters about any chosen mean value. Depolarized backscatter data for the test site at 5.7–68 cm are proportional to the rms height at the wavelength scale, mirroring a similar trend for continuous rough rocky surfaces. An empirical model relating rms height to depolarized backscatter coefficient appears to well describe the behavior of strewn surfaces. The polarized echoes are consistent with Mie scattering from surface rocks for a reasonable choice of dielectric properties, but the number of free parameters and the interaction of the scatterer and surface yields weak remote-sensing roughness or dielectric constraints. While depolarized backscatter data provide robust estimates of the rms height for continuous and discrete roughness populations, their use in Mars landing site planning is model-dependent. For single-wavelength data, we cannot uniquely determine the size-frequency distribution and the maximum rock diameter. Dual-wavelength observations, in the S- to P-band range, may better constrain the surface properties. © 2001 Academic Press

Key Words: Mars, surface, radar.

I. INTRODUCTION

Radar remote sensing of planetary surfaces requires models that relate measured echoes to the statistical properties of the target at horizontal and vertical scales comparable to the illuminating wavelength. There are two general classes for such surface descriptions. Continuous surfaces are those for which the height distribution about some mean elevation is characterized by a random process, often with a self-affine (power-law) relationship between the horizontal and vertical scales. The second type of surface is characterized by a population of discrete scattering objects on or within a supporting medium. Rock-strewn surfaces are an example of such a discrete population, and occur in a variety of geologic settings (e.g., crater ejecta, explosive volcanic deposits, and outwash fans). This type of surface is particularly relevant to current radar studies of Mars, but is also applicable to the Moon, Mercury, and Venus.

The size-frequency distribution of rocks determines the radar scattering properties of a strewn surface, but the relationship between the rock population, surface height statistics, and radar returns in the polarized and depolarized modes has not been examined in detail. Much of the early work in this field focused on the Moon, for which Surveyor panoramic photos provide ground-truth measurements of the surface rock population. Burns (1969) made one of the earliest efforts to relate radar backscatter to regolith subsurface properties. Thompson *et al.* (1970) and Pollack and Whitehill (1972) used a Mie scattering model for the regolith to determine the likely roles of surface and subsurface scattering in 70-cm radar echoes; Campbell *et al.* (1997) used high-resolution 70-cm images and multispectral data for mineralogy to further refine these conclusions.

Mars has also been the target of numerous radar studies (summarized in Simpson *et al.* 1992a) and many areas of the planet appear to be characterized by rock-strewn surfaces (Christensen 1986). Only recently, however, have imaging techniques permitted measurement of the depolarized radar backscatter coefficient for relatively small areas on the surface (e.g., Harmon *et al.* 1992b, 1999). Initial efforts to model the diffuse scattering cross section for Mars employed the Mie approximation for spheres and a differential rock size-frequency distribution (Harmon and Ostro 1985). Baron *et al.* (1998) used a finite difference time-domain electromagnetic simulation to model the scattered field for surface and subsurface rocks at the *Viking Lander* sites. Golombek *et al.* (1997, 1999) compared observations at the *Mars Pathfinder* site with near-nadir polarized-sense radar echoes obtained during mission planning (Haldemann *et al.* 1997). Planning for future landings will likely

38

continue to include assessment of the surface properties of potential sites from Earth-based radar data.

In this paper, we first discuss the relationship between differential rock size-frequency distributions and standard statistical surface height parameters. We then present a field site in Hawaii and its corresponding roughness statistics. Synthetic rock populations are used to demonstrate the dependence of height statistics on the population scaling coefficients and the maximum rock diameter. Based on AIRSAR data for the Hawaii field site, we test the predictions of Mie scattering theory and an empirical model for depolarized radar echoes against actual observations. Finally, we compare model predictions for the *Viking* landing sites to measured rock abundance, and assess the utility of radar data for remote estimation of surface properties.

II. QUANTIFYING SURFACE ROUGHNESS

A. Basic Statistical Descriptions

Surface distributions of discrete rocks are typically described by a power-law differential size-frequency relationship as a function of diameter d,

$$n(d) = C_p d^\beta \qquad (1)$$

with units of number per unit area per unit diameter (m^{-3}) (e.g., Turcotte 1992). Golombek and Rapp (1997) propose that an exponential function may better fit observed rock distributions, particularly at the largest sizes:

$$n(d) = C_e e^{\alpha d}. \qquad (2)$$

In describing natural surfaces, both functions may be constrained to a minimum and maximum applicable diameter, d_{min} and d_{max}.

Many radar scattering models for natural surfaces use descriptive statistical parameters such as the root-mean-square (rms) height or rms slope. For a continuous random rough surface, such as a lava flow, the standard deviation or rms of surface height, relative to the local mean, is dependent on the length scale, L, over which it is measured. Many natural surfaces exhibit increasing rms height with increasing length scale, often following a power-law fractal behavior,

$$h_a(L) = C_h L^H, \qquad (3)$$

where H is the Hurst exponent and C_h is an anchoring parameter corresponding to the rms height at unit scale (Shepard *et al.* 1995). The Hurst exponent is related to the fractal dimension, D, by $H = 2 - D$ for a two-dimensional profile and by $H = 3 - D$ for a three-dimensional surface. The rms height is independent of the horizontal step size, Δx, used to create a profile of length L. A value of $H = 0$ corresponds to a stationary surface, for which changes in the horizontal scale size have no effect on the vertical roughness component. Brownian or random walk processes have $H = 0.5$.

The rms slope is defined as the ratio of the surface rms elevation difference, relative to an arbitrary point, to the horizontal step size over which it is measured. The former quantity is termed the Allan deviation (or structure function),

$$\nu(\Delta x) = \sqrt{\langle (h(x) - h(x + \Delta x))^2 \rangle}, \qquad (4)$$

where $h(x)$ is the height of the surface at a particular location. The rms slope, s, is given by

$$s = \frac{\nu(\Delta x)}{\Delta x} \qquad (5)$$

For a fractal surface, the Allan deviation, and thus the rms slope, has a power-law dependence on step size,

$$s = \frac{C_a \Delta x^H}{\Delta x} = C_a \Delta x^{H-1} \qquad (6)$$

and C_a is an anchoring parameter related to the Allan deviation at unit scale. Note that the Allan deviation is independent of the length scale or area over which it is calculated.

Where the rms height characterizes elevation differences relative to a local mean, the Allan deviation measures the distribution of height differences relative to a chosen point that may lie above or below the mean. The Allan deviation is a robust method of quantifying roughness on a continuous surface, because values of ν can be obtained down to the smallest step size measured. For a strewn surface, however, it is difficult to relate the Allan deviation (and thus the rms slope) to the size-frequency function, primarily because the slope distribution has abrupt vertical tilts at the edge of any perched rock. We will therefore focus on the rms height as a descriptive parameter.

While scattering by spheres is a relatively tractable problem, rocks on or within a planetary regolith typically display a range of ellipsoidal shapes. Nonspherical rock shape is likely to be a primary source of radar depolarization from strewn fields, with more limited contributions from multiple scattering between the surface and the rocks. In studies of rock distributions, a commonly used parameter is sphericity, defined as the ratio of minimum (minor axis) to maximum (major axis) diameter, d_{minor}/d_{major}. This parameter has a range from unity (spheres) to 0 (needles), although real rocks will not approach the lowest possible values.

B. Properties of Power-Law and Exponential Distributions

For a power-law distribution of rock diameter, the rms height is a function of C_p, β, d_{min}, and d_{max}. While the distribution predicts that even extremely large rocks will eventually occur if the surface area is adequately large, in practice mechanical or other constraints tend to limit the upper diameter value. The maximum rock diameter for a site is defined here as that for which the surface population is consistent with the power-law function; rocks larger than d_{max} may still occur, but far less frequently than predicted by (1).

We first derive a value for h_o for the case where the length scale of interest is much larger than the largest rock in the field ($L \gg d_{max}$). In this case, the surface is stationary. For simplicity, the rocks are assumed to be spherical. The area-weighted, summed height of all points on the surface of a perched sphere of diameter d, stepping out in distance, x, from the center is

$$2\pi \int_0^{d/2} x \left(\frac{d}{2} + \sqrt{\left(\frac{d}{2}\right)^2 - x^2} \right) dx = \frac{5\pi}{24}d^3, \qquad (7)$$

and the area-weighted sum-squared height is

$$2\pi \int_0^{d/2} x \left(\frac{d}{2} + \sqrt{\left(\frac{d}{2}\right)^2 - x^2} \right)^2 dx = \frac{17\pi}{96}d^4. \qquad (8)$$

We next integrate over the total rock population and use the binomial approximation for the standard deviation to obtain

$$h_o \approx \left(\left[\frac{17C_s\pi}{96(5+\beta)} \left(d_{max}^{5+\beta} - d_{min}^{5+\beta} \right) \right] \right.$$
$$\left. - \left[\frac{5C_s\pi}{24(4+\beta)} \left(d_{max}^{4+\beta} - d_{min}^{4+\beta} \right) \right]^2 \right)^{1/2}. \qquad (9)$$

The area does not enter into the final answer, as the differential rock population normalizes the fraction of surface covered by rocks of each diameter. Many rock-strewn surfaces have values of β between -2.5 and -3.5, and typically $d_{max} \gg d_{min}$. In this case, the first-order approximations for (9) are

$$h_o(\beta = -3.5) \approx 0.61 d_{max}^{0.75} \sqrt{C_s} \qquad (10)$$

$$h_o(\beta = -2.5) \approx 0.47 d_{max}^{1.25} \sqrt{C_s}. \qquad (11)$$

These are the maximum possible values for the rms height of a power-law distribution, and again apply to stationary surface areas (or profile lengths) much larger than the maximum rock diameter.

The exponential size-frequency function has the advantage of a closed-form solution when integrated over the diameter range from 0 to ∞. Using (7) and (8), the maximum rms height is

$$h_o \approx \left[\frac{-17\pi C_e}{4\alpha^5} - \frac{25\pi^2 C_e^2}{16\alpha^8} \right]^{1/2}. \qquad (12)$$

Provided $|\alpha|$ is relatively large, this value approaches

$$h_o \approx 3.65 \sqrt{C_e} \alpha^{-5/2}. \qquad (13)$$

C. Synthetic Surface Models

The implication of (9) and (13) is that any remote-sensing analysis must consider at least a two- (α, C_e) or three-parameter model (β, C_p, $d_{max} \gg d_{min}$) for the surface in attempting to fit observed radar data. The problem is more complicated in that radar measurements are sensitive to surface roughness on horizontal scales comparable to that of the illuminating wavelength, λ. In many cases, this scale length is smaller than that required for the surface to appear stationary (i.e., λ does not satisfy $\lambda \gg d_{max}$), and the rms height will be less than the maximum possible value. An analytical solution to the rms height for these shorter scale lengths as a function of surface parameters is not tractable, so we must rely on simulations to examine the functional dependence of roughness on horizontal scale.

To determine the variability of surface height parameters with rock field statistics, we created synthetic topography models. Each model is an 8000×8000 array of 0.002×0.002 m^2 elements (a total area of 256 m^2). Spherical rocks corresponding to the chosen size-frequency function are placed on this grid at random, starting from the largest radii, and subsequent rocks are not permitted to overlap existing ones. The bin width for rock diameter is permitted to vary, since much larger bins are required to obtain a single sphere at larger sizes. The resulting surface topography maps for each choice of parameters are then used to determine h_o as a function of horizontal scale.

III. FIELD MEASUREMENTS AND RADAR DATA

A. Rock Size-Frequency Distribution

Our field site is a rock-strewn surface produced by the 1924 phreatomagmatic eruption of Kilauea Volcano, Hawaii (Fig. 1). This eruption, driven by the explosive mixing of groundwater and magma, produced a field of comminuted debris surrounding Halemaumau crater. The site is close to the west edge of Halemaumau, between the pit crater and the distal end of a pahoehoe lava flow from the 1974 eruption (Fig. 2). The background matrix is comprised of fine debris that has been partially welded into a friable crust. Beneath the 1924 deposit are smooth pahoehoe lava flows dating from 1919 to 1921.

We measured the rock population within a sample area 10×10 m in extent. This area was further subdivided into a "high-resolution" 4×10 m region, and a "low-resolution" 6×10 m region. In both areas, we measured the major and minor axes of each rock above a certain cutoff diameter value. To avoid truncation errors in the statistical analysis, we also measured all rocks that fell slightly below the threshold value, and discarded these in later work. The minimum diameter for the high-resolution area was 5 cm, and 10 cm for the low-resolution area. In the terminology of Baron *et al.* (1998), all of these rocks are "perched" on the background surface, with only the smallest rocks significantly embedded in the friable matrix (Fig. 3). A total of 735 total rocks were measured in the high-resolution area and 223 in the low-resolution area. The major-axis and minor-axis diameters for each rock were averaged; we then binned the high-resolution rock count using 2-cm intervals of diameter, and the low-resolution count using 4-cm intervals. Bins containing less than 10 rocks were ignored in fitting distribution functions. The field site differential distribution and best-fit power-law and

FIG. 1. Photo of the Hawaii field site. The boundaries of the 10 × 10 m sample region are shown by the white highlighted line.

exponential functions are shown in Fig. 4. Table I compares the power-law fit with published results for the *Viking* Mars landing sites (Baron *et al.* 1998).

The largest single rock within our study area has a mean diameter of 44 cm. The largest bin for which the power-law and observed rock counts are similar, however, covers the range from 26 to 30 cm. Bins above this diameter range have many fewer observed rocks than predicted by the best-fit power law function. We thus take a value of $d_{max} \sim 28$ cm as the limit of validity for the power-law model. The exponential model fits

FIG. 2. C-band (5.7-cm wavelength) AIRSAR HV-polarization radar image of Kilauea caldera. West is at the top. The white arrow shows the location of the field test site.

FIG. 3. Representative surface area within the Hawaii test site. Ruler is 30 cm in length.

relatively well for $d > 8$ cm, but greatly underestimates the rock population for smaller scales.

B. Radar Data

AIRSAR imaging radar data for the Kilauea field site provide calibrated values of radar backscatter, in multipolarization format, at incidence angles of ~30°–50° for wavelengths of
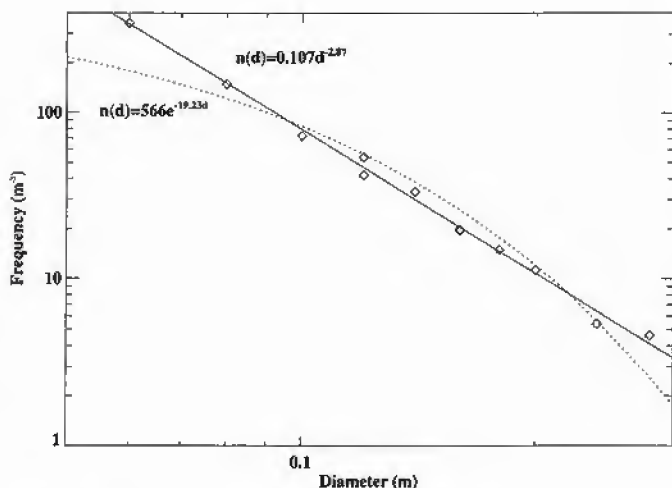

FIG. 4. Differential rock diameter distribution for the Hawaii test site, with best-fit power-law (solid line) and exponential (dashed line) functions.

5.7 (C band), 24 (L band), and 68 cm (P band). We calculated mean backscatter values for the study site, using three radar image swaths to cover the range of incidence angles. HH and HV backscatter coefficients for the test site are plotted in Fig. 5. The HV data follow a power-law trend with wavelength, similar to the self-affine scaling observed for continuous rough lava flows (Campbell and Shepard 1996). Recent high-resolution Mars image data are collected in the circular-sense depolarized mode (LL or RR polarization), at a wavelength of 12.6 cm. Assuming self-affine scaling in the backscatter values, we may estimate an S-band echo from the AIRSAR data using

$$\sigma_{dB}^{o}(12.6 \text{ cm}) = 0.47\sigma_{dB}^{o}(5.7 \text{ cm}) + 0.53\sigma_{dB}^{o}(24 \text{ cm}) \qquad (14)$$

Table II presents interpolated S-band backscatter coefficients for

TABLE I
Differential Size-Frequency Functions for Test Sites

Site	Differential distribution (m^{-3})
Hawaii	$n(d) = 0.107d^{-2.87}$
Viking 1	$n(d) = 0.019d^{-3.34}$
Viking 2	$n(d) = 0.088d^{-2.54}$

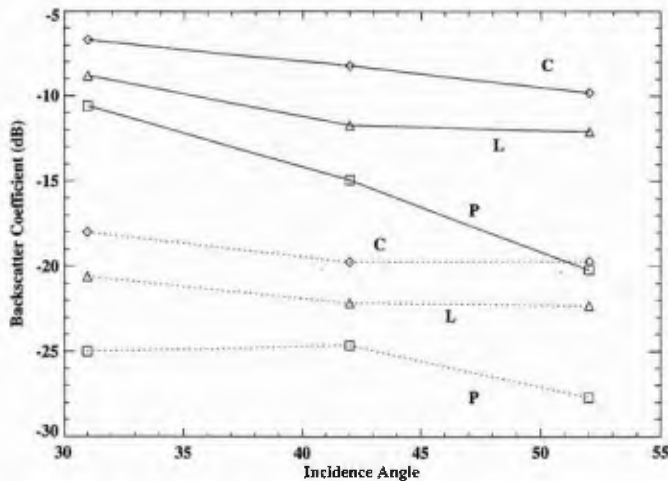*Note.* Value for Mars surface rock distribution from Baron *et al.* (1998).

FIG. 5. Radar backscatter data in the HH (solid lines) and HV (dashed lines) polarization modes for the Hawaii test site. The three wavelengths are labeled as C (5.7 cm), L (24 cm), and P (68 cm).

the test site, along with the 12.6-cm LL data for the *Viking* sites compiled by Baron *et al.* (1998).

IV. INTERPRETATION OF RADAR ECHOES FROM ROCK STREWN SURFACES

A. Polarized Echoes

Radar echoes from rock-strewn planetary surfaces or rocky regoliths have often been modeled using Mie scattering theory (e.g., Thompson *et al.* 1970, Pollack and Whitehill 1972, Harmon and Ostro 1985, Campbell *et al.* 1997). The Mie backscatter cross section of any single sphere is dependent upon the complex relative dielectric constant of the scatterer and the surrounding matrix, and the ratio of radar wavelength in the matrix to the radius of the sphere (Bohren and Huffman 1983). For perched rocks, this is not a rigorously correct solution for the

TABLE II

Same-Sense 12.6-cm Circular-Polarized Radar Echoes for Test Sites

Site	Incidence angle	σ^o (dB)
Hawaii	31°	−15.4
	42°	−16.5
	52°	−16.3
Viking 1	36°	−17.2
	29°	−15.0
Viking 2	54°	−17.4
	60°	−19.4
	47°	−18.9
	51°	−18.5

Note. Data for the *Viking* sites compiled by Baron *et al.* (1998) from previous authors. The Hawaii S-band values are interpolated from 6- and 24-cm data using (14).

scattered field, since the presence of the supporting dielectric interface violates the Mie assumption of a scatterer embedded in a homogeneous medium. Baron *et al.* (1998) address this issue in their numerical modeling, and show that the underlying surface exerts a considerable influence on radar echoes from perched and partially buried rocks. Likewise, rocks on natural surfaces are not spherical, so a backscatter coefficient derived from the Mie model is only an approximation to echoes from ellipsoidal rocks of similar volume.

Despite these problems, the Mie model is often taken as a starting point to estimate polarized backscatter from a surface, so we used the rock count and AIRSAR data to compare model predictions to the observed echoes. The Mie cross section for the rock site was determined by numerically integrating over a power-law rock distribution from d_{min} to d_{max}, for rocks with complex dielectric constant (ε', ε''). We further assume that the rocks are suspended in free space, which maximizes the calculated echoes. Integrating over the distribution in small radius increments avoids difficulties with rapidly fluctuating resonant echoes, especially at lower loss tangent (tan $\delta = \varepsilon''/\varepsilon'$) values. We examined two cases that bracket a reasonable dielectric range for dry rocks (Ulaby *et al.* 1988): (a) low dielectric, high loss ($\varepsilon' = 3.0$, tan $\delta = 0.100$), (b) high dielectric, low loss ($\varepsilon' = 8.0$, tan $\delta = 0.002$). Lossless rocks have higher backscatter values, but such materials do not occur on planetary surfaces. We set $d_{min} = 0.005$ m in all cases, and tested d_{max} values of 0.30–1.0 m.

Figure 6 shows the Mie backscatter coefficient as a function of illuminating wavelength for the test site power-law distribution at the two endmember dielectric values. For comparison, the field-site HH data at 42° incidence are shown by the asterisks. The low-dielectric, high-loss case (dotted lines) underestimates the C-L band echoes, and only matches the P-band case when $d_{max} = 1.0$ m. The high-dielectric, low-loss case (solid lines)
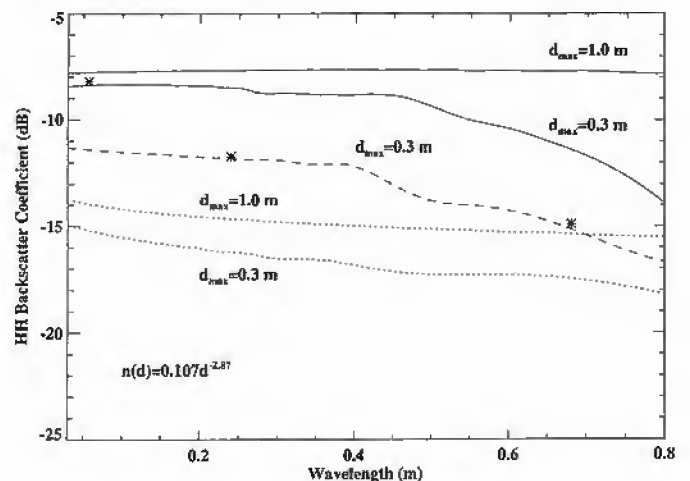

FIG. 6. Radar echoes for a power-law distribution of spheres in free space corresponding to the Hawaii test site. Solid lines correspond to ($\varepsilon' = 8.0$, tan $\delta = 0.002$), dotted lines to ($\varepsilon' = 3$, tan $\delta = 0.10$), dashed line to ($\varepsilon' = 6$, tan d $= 0.01$). Asterisks represent HH echoes from Hawaii site at 42° incidence.

matches the C-band echoes for $d_{max} \sim 0.5$ m, but greatly overestimates the L- and P-band values. The dashed line shows the backscatter for $\varepsilon' = 6$, $\tan \delta = 0.01$, which fits quite well in the range 24–68 cm. No values for the dielectric constant and d_{max} yield a good match to the Hawaii data at all three wavelengths. The higher C-band echo may be attributable to scattering by the slightly rough surface between the sampled rocks. Note that for rock distributions with $\beta \sim -3$ and moderate real dielectric constant and loss tangent, the model-predicted radar echo is nearly wavelength-independent when $\lambda < d_{max}$, consistent with the lunar work of Burns (1970).

These results show that Mie scattering is at least a reasonable approximation for polarized echoes, and may be useful in predicting backscatter when the rock size-frequency distribution is known and we wish to assess, for example, the relative roles of surface and subsurface radar scattering. The Hawaii data suggest, however, that processes such as interaction of the sphere and surface affect the polarized return, and create the angular dependence in power that cannot be modeled using the Mie approach (Fig. 5). While a Mie scattering model with appropriate parameters may qualitatively reproduce some aspects of the radar observations, it is thus unlikely that polarized backscatter measurements can significantly constrain both rock dielectric properties and size-frequency statistics.

B. Depolarized Echoes

Depolarized radar echoes are often attributed to a combination of single scattering by irregular objects and surface multiple scattering. The depolarization properties of continuous rough surfaces, such as lava flows, are most consistent with the former mechanism (Campbell *et al.* 1993). In particular, the circular- and linear-sense depolarized echoes (LL and HV) from lava flows typically follow a 2 : 1 scaling relationship over the wavelength range from 6 to 24 cm. This type of scaling is consistent with echoes from randomly oriented dipole-like features. On a surface comprised of discrete rocks, depolarization may occur due to single scattering from ellipsoidal shapes, discontinuities, or sharp edges on rocks, or from multiple-scattering interactions between the rocks and the ground. Multiple scattering between rocks seems unlikely unless the viewing geometry approaches grazing incidence.

Campbell and Shepard (1996) showed that changes in the depolarized echo from lava flows as a function of the radar wavelength mirrored the self-affine (fractal) roughness properties of the surface. The depolarized echo was related to rms height through an empirical model,

$$h_o(\lambda) \approx 0.24\lambda \sqrt{-\ln\left(1 - \frac{\sigma_{HV}^o}{0.04 \cos \phi}\right)} . \qquad (15)$$

where λ is the illuminating wavelength. The coefficient in (15) differs from that of Campbell and Shepard (1996), as more robust methods for calculating h_o show that the previously published
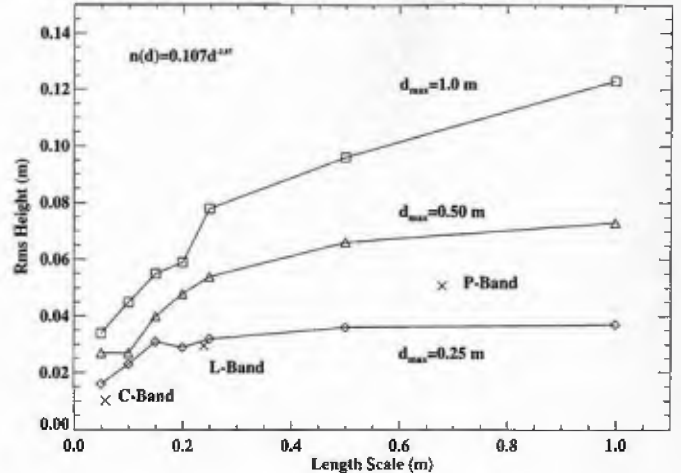

FIG. 7. Plot of rms height versus horizontal scale length for simulated rock populations, corresponding to the Hawaii field site statistics, as a function of d_{max}. The crosses denote values predicted by the observed HV backscatter at 5.7-, 24-, and 68-cm wavelengths using (15).

values are systematically low. This model assumes that the effective reflectivity of the surface component that contributes to radar scattering is relatively uniform.

The Hawaii site data may be used to test whether this empirical fit is also valid for rock-strewn surfaces. The HV backscatter data for the field site (Fig. 5) exhibit a self-affine (power-law) dependence on λ, and the LL and HV data at all wavelengths have an approximately 2 : 1 scaling behavior. Both behaviors are similar to those of continuous rough lava surfaces. As a further test, we determined the rms height of synthetic rock-strewn surfaces with the corresponding differential distribution and varying d_{max}, and compared these h_o values with the predictions of (15). Figure 7 shows that we can obtain a close match between synthetic surfaces and the model predictions for 6–24 cm wavelength when $d_{max} \sim 25$ cm, relative to the maximum discussed above of 26–30 cm. The best-fit value for d_{max} is higher at P-band, possibly due to additional echo power arising from subsurface volume scattering. For data at 6–24 cm wavelengths, it thus appears that the empirical model given by (15) provides a reasonable estimate of the rms height of a rock-strewn surface.

V. MARS LANDING SITE ANALYSIS

A. Rock Distributions and Sphericity

Baron *et al.* (1998) revised earlier rock size-frequency distributions for the *Viking* lander sites (Table I). Their histograms suggest that the maximum diameter for which the power-law distributions apply is <0.50 m. While larger rocks occur at both sites, they are much less abundant than predicted by a power-law function; these larger rocks are again better represented by an exponential distribution. The Arecibo backscatter data, due to the method used to normalize the scattering area over the north–south imaging ambiguity, are lower bounds on the true
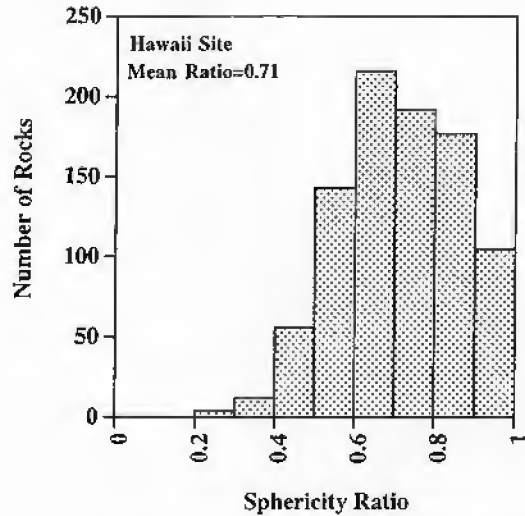
FIG. 8. Histogram of rock sphericity values for the Hawaii site.

backscatter coefficient (Harmon 1997). We further assume that the S-band HV backscatter coefficient may be approximated by LL/2 (Campbell *et al.* 1993).

Figure 8 shows the histogram of sphericity for all rocks in our Hawaii site. The mean ratio, S, is 0.71 ± 0.16, similar to values for perched rocks found by Baron *et al.* (1998) at the *VL1* (0.73 ± 0.17) and *VL2* (0.75 ± 0.14) sites. There is no correlation between rock size and sphericity in our data set. The very similar mean values for rock sphericity among these three sites suggest that S reflects some intrinsic statistical behavior rather than a unique property of the surface rocks. We carried out a number of empirical tests with various probability density functions, creating a weighted random collection of diameter values for each case and examining the dependence of ellipticity ratio on the mean and variance of the population. The data for Hawaii and Mars can be explained if the major- and minor-axis diameters of rocks follow a Rayleigh distribution about any chosen mean value. The probability density function for this case is

$$p(d) = 2\alpha d e^{-\alpha d^2}, \tag{16}$$

where α is an arbitrary scaling coefficient. The standard deviation of this distribution is approximately one-half its mean value of $\sqrt{\pi/4\alpha}$.

Figure 9 shows sphericity ratio histograms for two Rayleigh-distributed rock populations. Despite a threefold shift in the mean diameter of the rock population, the mean ratio value is ~0.6 in both cases, suggesting that the Hawaii and *Viking* site rock populations exhibit this type of size-frequency distribution at all average diameter values. The mean values of S near 0.7 for these sites are likely due to the fact that extremely elongate rocks readily break to form two objects with higher ratios, truncating the idealized sphericity population at the low end and

increasing the average value. These results may be useful in creating realistic ellipsoidal rock populations for finite-element modeling.

B. Correlation with Scattering Model

The *Viking* sites have quite similar backscatter properties. The average values of $\sigma_{LL}^o/(2\cos\phi)$, which we take as an estimate of the normalized HV echo, are -15.2 dB (*VL1*) and -16.2 dB (*VL2*). Using (15), these values imply rms heights at the 12.6-cm wavelength scale of 2.1 and 1.8 cm, respectively. Figure 10 shows the properties of synthetic surfaces with power-law distributions corresponding to the *Viking* sites for three values of d_{max}. The best fit to the S-band data for both sites lies in the range $d_{max} = 0.25$–0.50 m, consistent with the largest fully populated power-law bin. Given that the Arecibo values are likely
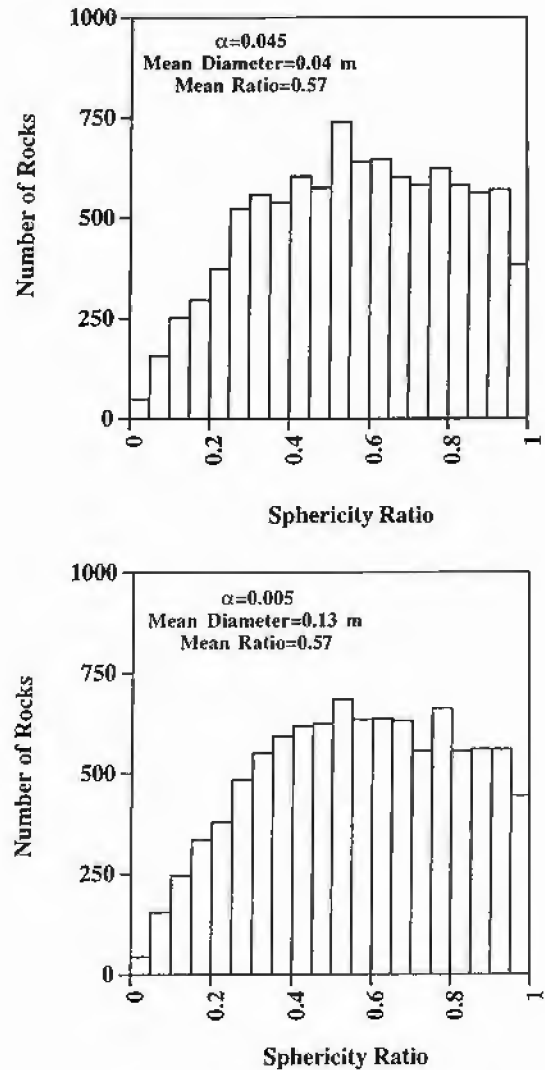

FIG. 9. Histograms of rock sphericity for two simulated rock populations, (a) and (b), with Rayleigh-distributed diameters. Note that despite a threefold change in the mean value of the rock diameter, the mean ratio remains ~0.6.
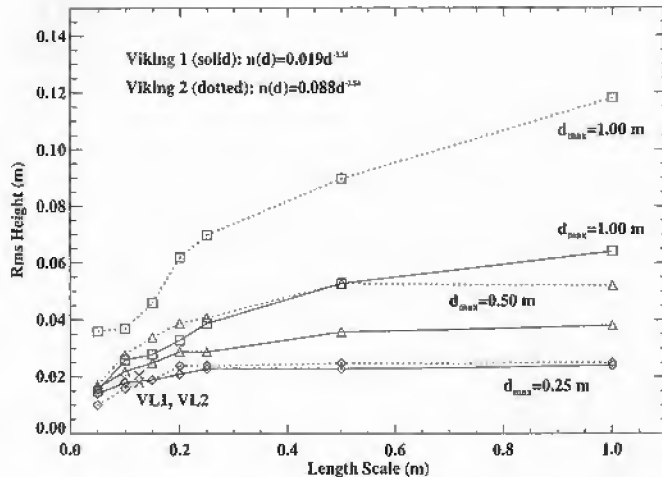
FIG. 10. Plots of rms height versus horizontal scale length for simulated rock populations, corresponding to the *Viking* sites, as a function of d_{max}. The crosses denote values predicted by the observed backscatter using (15).

lower bounds on the true backscatter coefficient, $d_{max} = 0.50$ m is probably the better estimate.

C. Remote-Sensing Applications

The results presented above suggest that depolarized radar scattering data provide robust estimates of the rms height of a surface at the wavelength scale for both continuous and discrete topography. The use of these data to remotely infer rock statistics is highly dependent upon limiting the number of free parameters. An exponential distribution function, while attractive for representing the larger rocks on a surface, underestimates the population of smaller rocks that strongly contribute to radar scattering. Using a power-law function, this means that we have a three-component model (β, d_{max}, C_p) to describe surface roughness. Obviously, a measurement of backscatter at a single wavelength leaves a very wide family of possible solutions. For example, an rms height of 2 cm at the 12.6-cm horizontal scale (i.e., *VL1* and *VL2*) corresponds to the following functions if we assume $d_{max} = 0.3$ m: $n(d) = 0.015d^{-3.5}$, $0.09d^{-3.0}$ and $0.11d^{-2.5}$. The coefficient for any given value of β changes as a function of d_{max}.

If we wish to estimate the rock abundance at various sites on Mars (or other planets), data at multiple radar wavelengths are a necessity. Given the dependence of σ^o on the ratio of surface roughness to radar wavelength (15), it is most effective to obtain data in the S- to P-band range. Shorter wavelengths tend to saturate on relatively low-roughness surfaces, leading to little discrimination among terrains. Observations of Mars at wavelengths longer than 12.6 cm will almost certainly require an orbital SAR, due to limitations on Earth-based systems. Data for two wavelengths can offer improved constraints on the rock size-frequency distribution, and long wavelengths (>50 cm) can be most helpful in identifying the maximum populated diameter bin. While radar data cannot uniquely quantify the largest few rocks in an area, they can be used to assess roughness at submeter scales for lander safety or rover trafficability studies.

REFERENCES

Baron, J. E., R. A. Simpson, G. L. Tyler, H. J. Moore, and J. K. Harmon 1998. Estimation of Mars radar backscatter from measured surface rock populations. *J. Geophys. Res.* **103**, 22,695–22,712.

Bohren, C. F., and D. R. Huffman 1983. *Scattering and Emission from Small Particles.* Wiley, New York.

Burns, A. A. 1969. Diffuse component of lunar radar echoes. *J. Geophys. Res.* **74**, 6553–6566.

Burns, A. A. 1970. On the wavelength dependence of radar echoes from the Moon. *J. Geophys. Res.* **75**, 1467–1482.

Campbell, B. A., and M. K. Shepard 1996. Lava flow surface roughness and depolarized radar scattering. *J. Geophys. Res.* **101**, 18,941–18,951.

Campbell, B. A., R. E. Arvidson, and M. K. Shepard 1993. Radar polarization properties of volcanic and playa surfaces: Applications to terrestrial remote sensing and Venus data interpretation. *J. Geophys. Res.* **98**, 17,099–17,113.

Campbell, B. A., B. R. Hawke, and T. W. Thompson 1997. Long-wavelength radar studies of the lunar maria. *J. Geophys. Res.* **102**, 19,307–19,320.

Christensen, P. R. 1986. The spatial distribution of rocks on Mars. *Icarus* **68**, 217–238.

Golombek, M., and D. Rapp 1997. Size-frequency distributions of rocks on Mars and Earth analog sites: Implications for future landed missions. *J. Geophys. Res.* **102**, 4117–4129.

Golombek, M., H. J. Moore, A. F. C. Haldemann, T. J. Parker, and J. T. Schofield 1999. Assessment of Mars Pathfinder landing site predictions. *J. Geophys. Res.* **104**, 8585–8595.

Golombek, M., and 13 colleagues 1997. Overview of the Mars Pathfinder Mission and assessment of landing site predictions. *Science* **278**, 1743–1748.

Haldemann, A. F. C., D. L. Mitchell, R. F. Jurgens, M. A. Slade, and D. O. Muhleman 1997. Mars Pathfinder landing site assessment with Goldstone delay-Doppler and CW radar experiments. *J. Geophys. Res.* **102**, 4097–4106.

Harmon, J. K. 1997. A radar study of the Chryse region, Mars. *J. Geophys. Res.* **102**, 4081–4095.

Harmon, J. K., and S. J. Ostro 1985. Mars: Dual-polarization radar observations with extended coverage. *Icarus* **62**, 110–128.

Harmon, J. K., R. E. Arvidson, E. A. Guinness, B. A. Campbell, and M. A. Slade 1999. Mars mapping with delay-Doppler radar. *J. Geophys. Res.* **104**, 14,065–14,090.

Harmon, J. K., M. A. Slade, and R. S. Hudson 1992b. Mars radar scattering: Arecibo/Goldstone results at 12.6- and 3.5-cm wavelengths. *Icarus* **98**, 240–253.

Harmon, J. K., M. P. Sulzer, P. J. Perillat, and J. F. Chandler 1992a. Mars radar mapping: Strong backscatter from the Elysium basin and outflow channel. *Icarus* **95**, 153–156.

Pollack, J. B., and L. Whitehill 1972. A multiple-scattering model of the diffuse component of lunar radar echoes. *J. Geophys. Res.* **77**, 4289–4303.

Shepard, M. K., R. A. Brackett, and R. E. Arvidson 1995. Self-affine (fractal) topography: Surface parameterization and radar scattering. *J. Geophys. Res.* **100**, 11,709–11,718.

Simpson, R. A., J. K. Harmon, S. H. Zisk, T. W. Thompson, and D. O. Muhleman 1992. Radar determination of Mars surface properties. In *Mars* (H. Kieffer, B. Jakosky, C. Snyder, and M. Mathews, Eds.), pp. 652–685. Univ. of AZ Press, Tucson.

Thompson, T. W., J. B. Pollack, M. J. Campbell, and B. T. O'Leary 1970. Radar maps of the Moon at 70-cm wavelength and their interpretation. *Radio Science* **5**, 253–262.

Turcotte, D. L. 1992. *Fractals and Chaos in Geology and Geophysics.* Cambridge Univ. Press, New York.

Ulaby, F. T., T. Bengal, J. East, M. C. Dobson, J. Garvin, and D. Evans 1988. Microwave dielectric spectrum of rocks, University of Michigan Radiation Laboratory, Report 23817-1-T.